Deformable MR-CBCT prostate registration using biomechanically constrained deep learning networks

Yabo Fu,
Department of Radiation Oncology, Emory University, Atlanta, GA, USA

Tonghe Wang,
Department of Radiation Oncology, Emory University, Atlanta, GA, USA

Winship Cancer Institute, Emory University, Atlanta, GA, USA

Yang Lei
Department of Radiation Oncology, Emory University, Atlanta, GA, USA

Pretesh Patel, **Ashesh B. Jani**, **Walter J. Curran**, **Tian Liu**, **Xiaofeng Yang**[a]
Department of Radiation Oncology, Emory University, Atlanta, GA, USA

Winship Cancer Institute, Emory University, Atlanta, GA, USA

Abstract

Background and purpose: Radiotherapeutic dose escalation to dominant intraprostatic lesions (DIL) in prostate cancer could potentially improve tumor control. The purpose of this study was to develop a method to accurately register multiparametric magnetic resonance imaging (MRI) with CBCT images for improved DIL delineation, treatment planning, and dose monitoring in prostate radiotherapy.

Methods and materials: We proposed a novel registration framework which considers biomechanical constraint when deforming the MR to CBCT. The registration framework consists of two segmentation convolutional neural networks (CNN) for MR and CBCT prostate segmentation, and a three-dimensional (3D) point cloud (PC) matching network. Image intensity-based rigid registration was first performed to initialize the alignment between MR and CBCT prostate. The aligned prostates were then meshed into tetrahedron elements to generate volumetric PC representation of the prostate shapes. The 3D PC matching network was developed to predict a PC motion vector field which can deform the MRI prostate PC to match the CBCT prostate PC. To regularize the network's motion prediction with biomechanical constraints, finite element (FE) modeling-generated motion fields were used to train the network. MRI and CBCT images of 50 patients with intraprostatic fiducial markers were used in this study. Registration results were evaluated using three metrics including dice similarity coefficient (DSC), mean surface distance (MSD), and target registration error (TRE). In addition to spatial registration accuracy, Jacobian

---

[a]Author to whom correspondence should be addressed. xiaofeng.yang@emory.edu.

determinant and strain tensors were calculated to assess the physical fidelity of the deformation field.

Results: The mean and standard deviation of our method were 0.93 ± 0.01, 1.66 ± 0.10 mm, and 2.68 ± 1.91 mm for DSC, MSD, and TRE, respectively. The mean TRE of the proposed method was reduced by 29.1%, 14.3%, and 11.6% as compared to image intensity-based rigid registration, coherent point drifting (CPD) nonrigid surface registration, and modality-independent neighborhood descriptor (MIND) registration, respectively.

Conclusion: We developed a new framework to accurately register the prostate on MRI to CBCT images for external beam radiotherapy. The proposed method could be used to aid DIL delineation on CBCT, treatment planning, dose escalation to DIL, and dose monitoring.

1. INTRODUCTION

Prostate cancer is the second most common malignant disease, which accounts for 28% of newly diagnosed cancers in men each year around the world.[1] Radiation therapy such as external beam radiotherapy (EBRT), brachytherapy, and a combination of the two is commonly used to treat prostate cancer. In radiotherapy, the entire prostate is often prescribed to a single dose level since prostate cancer is presumed to be multifocal.[2] However, studies have shown that dominant intraprostatic lesion (DIL) is the site that contains the largest and/or the highest grade of lesion. Though the volume of DIL is typically <10% of the entire prostate volume, DIL is the most common tumor recurrence site after radiation therapy.[2,3] Several studies have shown that dose escalation to the DIL during radiotherapy is beneficial to tumor control.[2,3] However, it is difficult to accurately delineate the DIL on CT due to its low soft tissue contrast inside the prostate. In contrast to CT, multiparametric MRI (mpMRI) has superior soft tissue contrast inside the prostate. Therefore, it has become a standard to detect DIL on mpMRI in prostate radiotherapy.[3–6] In order to propagate the DIL delineation from mpMRI to CT, accurate mpMRI-CT image registration is needed. However, it is very challenging to register mpMRI with CT/CBCT on prostate because of (a) distinct appearances with inconsistent image intensities, (b) large prostate position shift and shape discrepancies due to varying rectum and bladder filling,[7] (c) poor CT/CBCT soft tissue contrast, and (d) poor CBCT image quality due to large photon scattering noise and artifacts. For these reasons, most studies on MRI-CT/CBCT registration are limited to rigid or affine registration,[8,9] and very few articles of nonrigid registration methods have been published.

Mutual information (MI) is generally used when performing multimodal image registration. McLaughlin et al. used MI-based method to register prostate MRI-CT post permanent seed implant in brachytherapy.[10] They showed that the registration is helpful to improve prostate contouring and postimplant dosimetry. Ciardo *et al.* used a B-spline MI-based method for MRI-CT image registration to propagate MRI-defined DIL to CT.[4] To enhance the image contrast of the organs-at-risk (OARs) that affect prostate position and shape, they increased

the intensity values of these organs by a fixed value prior to image registration. Commandeur et al. used prostate contours to aid MRI-CT registration.[11] A random forest classification was first used to detect prostate on CT images to generate probabilistic prostate contours. A similarity metric was defined to maximize the probability and collinearity between the normal of the MRI and CT contours. The markers position error after registration was on average 2.13 mm evaluated on gold seeds implant/calcification landmarks. They have outperformed a MI-based registration method by 7% in terms of Dice score. Intraprostatic fiducial markers/radiation seeds were also used to aid rigid registration between MR and CT images. Kunogi et al. rigidly aligned MRI and CT prostate images using prostate implant seed source locations by least square method.[12] Parker *et al.* used intraprostatic fiducial markers to rigidly register MRI and CT images.[13] They showed the feasibility of using intraprostatic fiducial markers, rather than bony structure markers for the registration. Aside from the MI-based deformable registration and the fiducial markers/ radiation seeds aided rigid registration, image synthesis techniques have also been employed for prostate MR and CT registration. Various image synthesis techniques were used to transform multimodal to unimodal image registration. Cao et al. proposed to use multi-target regression forest to perform both MRI-to-CT and CT-to-MRI image synthesis to handle the large appearance gaps between MRI and CT.[14] They have showed superior performance as compared to direct multimodal image registration. Fu et al. used a generative adversarial network to synthesize MRI from CT, and used the synthetic MRI (sMRI) as a surrogate of CT image in pelvic MRI-CT registration.[15]

Alternatively, organ surface registration could be used to bypass the lack of accurate image similarity measures in prostate multimodal image registration. For example, prostate surface registration has been used in MRI-TRUS image registration to provide MRI guidance in prostate biopsy and brachytherapy.[16–19] In contrast, surface registration has been explored much less for prostate MRI-CT/CBCT image registration. This maybe because prostate boundary is better defined in TRUS than in CT/CBCT. In radiotherapy, prostate is usually oversegmented on CT in order to cover the whole prostate. Studies have shown that manually delineated prostate volume on CT is on average 35% larger than that on MRI.[20] Recently, deep learning-based methods were proposed to provide superior prostate segmentation on CT/CBCT,[21] which enables prostate surface-based MRI-CT registration. One drawback of surface-based registration method is that it relies on mathematical models such as linear, bicubic, cubic and spline functions to interpolate the surface-driven deformations to the whole image domain. Due to the absence of control points within the prostate, these mathematical interpolation functions may introduce large deformation error inside the prostate. Finite element (FE) analysis is a powerful tool for soft tissue deformation modeling. FEM has improved the performance of nonrigid image registration in many medical simulation applications.[22,23] FEM has been investigated in MRI-MRI prostate registration,[24,25] MRI-TRUS prostate registration to model the prostate deformation induced by the endorectal coil and ultrasound probe.[16,17,26,27] They have shown promising results of using FEM to aid deformable prostate registration. Bladder, rectal filling, and patient setup condition could also cause prostate shape to change during the treatment process. FE analysis considers tissue stiffness property, boundary conditions, and biomechanical constraint to model the prostate deformation. However, FE model that consists of geometry

meshing, material property assignment, boundary condition definition, and so on usually requires substantial time and labor to build and solve, which prevent FE from being routinely used in the clinic.[16,17,28,29]

As artificial intelligence develops, many deep learning-based methods have been proposed for medical image processing such as segmentation,[30] registration,[31] synthesis,[32] and so on. Compared to traditional image processing methods, deep learning-based methods are generally faster and more robust to hyperparameter selection. The recent success of deep learning in medical image processing has inspired us to explore the possibility of using deep learning to replace FE modeling in biomechanically constrained image registration. To this end, we propose to use volumetric point cloud (PC) to represent the prostate gland and to use a PC matching network (PCMN) to learn the prostate deformation in FE modeling. Several studies have been proposed to use deep learning for PC processing. Qi et al. proposed a PointNet to classify and segment 3D PC.[33,34] Liu et al. employed a PC-based network called FlowNet3D to predict 3D scene flow between stereo and RGB-D images.[35] Aoki et al. proposed to combine PointNet and Lucas & Kanade (LK) algorithm for 3D PC rigid registration using deep learning.[36] In this study, we extended the usage of PC-based deep learning methods to medical image registration. Specifically, we trained a PCMN using FE-generated volumetric PC motion. Given two volumetric PC representing two prostates to be registered, the trained PCMN was able to predict the motion vector field of one PC to match the other. The predicted motion field was then used to deform the MR image in MRI-CBCT prostate registration. The contributions of this study are

1. An automatic MRI-CT prostate deformable image registration framework was developed by combining a CNN-based MRI prostate segmentation network, a CNN-based CBCT prostate segmentation network, and a volumetric PC matching network.

2. The volumetric PC matching network was trained using FE-generated PC motion vector field so that the trained network was able to implicitly apply the learned biomechanical constraints to prostate deformation during the registration.

3. A combination of motion vector prediction loss and Chamfer surface distance loss was used to train the PCMN.

2. MATERIALS AND METHODS

Flowchart of the proposed method is shown in Fig. 1. First, two convolutional neural networks (CNN), CNN_1[37] and CNN_2,[21] were used to segment the prostate from MRI and CBCT, respectively. To initialize the alignment, the MRI and CBCT were rigidly registered using MI-based registration. The rigidly aligned prostate masks were then meshed into surface point clouds (PCs) to represent the prostate shapes. The MRI and CBCT prostate surface PCs were then registered to establish PC correspondence between the two, which was used as nodal displacement boundary condition to drive prostate deformation in the FE model. The FE model was used to predict deformation within the prostate and to build volumetric PC correspondences. Taking the MRI and CBCT prostate volumetric PC as input, the proposed PC matching network (PCMN) was trained to predict the motion of MRI

prostate PC to both match the CBCT prostate shape and comply with the FE-generated motion vectors. In testing phase, prostates of a new MRI and CBCT pair were first segmented using the two CNNs, then meshed into tetrahedron elements to generate volumetric PC. It is not required for the meshing to have equal number of points in the two volumetric PCs since the network can automatically sample two subsets of PCs with equal number of points from the two volumetric PCs. The MRI and CBCT prostate volumetric PC were fed to the trained PCMN to perform PC matching between the two. MRI images was subsequently deformed using the predicted PC motion vector field.

2.A. Data acquisition

We retrospectively collected data from 50 patients with prostate cancer treated with proton radiotherapy. Each dataset has a series of mpMRI and multiple CBCT scans. The mpMRI scans include T1-weighted, T2-weighted, and diffusion-weighted MRIs, which were acquired on an Aera (Siemens, Germany) 1.5T scanner. The T1-weighted MRIs were scanned using a gradient recalled sequence (TR/TE: 6.9/2.39 ms, flip angle: 10°) with $1.3 \times 1.3 \times 1.3$ mm^3 voxel size. The T2-weighted MRIs were scanned using a spin echo sequence (TR/TE: 1600/166 ms, flip angle: 170°) with $1.0 \times 1.0 \times 1.0$ mm^3 voxel size. Multiple CBCT scans were taken prior to each fraction using Varian ProBeam CBCTsystem with $1.0 \times 1.0 \times 2.0$ mm^3 voxel size. Assuming that the larger time span between the CBCT and MRI, the greater possibility that the image content is different due to tumor shrinkage, patient weight loss, and physiological changes, we have chosen to register the MRI with the last fraction CBCT to demonstrate that the proposed method could be applied to CBCT across the entire treatment course. As a preprocessing step, all datasets were resampled to $1.0 \times 1.0 \times 1.0$ mm^3 voxel size. Institutional review board approval was obtained; no informed consent was required for this HIPAA-compliant retrospective analysis.

2.B. FE Modeling of prostate deformation

Since we aim to train a PCMN with implicit biomechanical awareness, FE analysis was used to generate prostate deformation during the registration which was then used to establish prostate volumetric PC correspondence for PCMN training. To build the FE model, we need to establish prostate boundary condition, assign prostate tissue property, and solve the nodal displacements within the prostate. These steps are described one by one in the following sections.

2.B.1. Prostate boundary condition establishment—Prostate was first segmented using two separately trained CNN models. A 3D fully convolutional network was developed using group dilated convolutional layers and trained using deep supervision to segment the prostate from MRI T2-weighted images. The network was trained using internal 40 MRI T2-weighted datasets and tested using a separate public dataset which include 50 T2-weighted prostate MRI. The average dice similarity coefficient (DSC) was 0.88 ± 0.05 for prostate segmentation. To segment the prostate on CBCT images, we trained another network which used both the original CBCT and synthetic MRI generated from the CBCT. The network was trained and tested on 100 patients' datasets and achieved an average DSC of 0.91 ± 0.08 for prostate segmentation. For details of prostate segmentation on MRI and CBCT, please refer to Wang et al.'s work[37] and Fu et al.'s work.[21] The prostate masks were then meshed

into around 5000 tetrahedron elements with around 1200 nodes. Around 5000 tetrahedron elements are considered enough for the FE to model the relatively small prostate gland. The average element size is around 0.005 ml for an average of 25 ml size prostate. We modeled the prostate deformation in FE using nodal displacement boundary conditions (BC). The nodal correspondences were obtained by nonrigidly registering the prostate surfaces between MRI and CBCT. The reasons of using nodal displacement BC are (a) external force to the prostate by its surrounding tissue/organs such as bladder and rectum was unavailable, (b) nodal displacement BC obtained by prostate surface registration could ensure that the MRI prostate shapes match the CBCT prostate shapes after FE deformation, which is desirable to train the PCMN. Image intensity-based rigid prostate registration was first performed to roughly align the mpMRI and CBCT images. Nonrigid surface registration was then performed to match the prostate surfaces from MRI with that from CBCTusing local rigid deformation. The local rigid deformation was performed by rigidly registering the nearby nodes N_i on MRI to the nearest local points on CBCT. Let v_i be the ith node from the MRI prostate surface, a set of nearby nodes N_i around v_i were then defined based on spatial and directional distances, denoted as $G_{N_i}^{mri}$. Local points on CBCT, denoted as G^{cbct} were selected as the nearest three points for each point in $G_{N_i}^{mri}$. The nonrigid surface registration was represented as a weighted summation of local rigid deformation around each node.[38]

$$m(v_i) = \sum_{j \in N_i} w_{ji}\big[R_j(v_i) + t_j(v_i)\big] \tag{1}$$

where $m(v_i)$ denotes the nodal motion vector of v_i, w_{ji} is a linear distance-based weights, R_j represents local rotation, and t_j represents local translation. The R_j and t_j were calculated by registering the local PC using MATLAB built-in function "procrustes." The nearby N_i surface nodes were surface points and selected using MATLAB built-in function "knnsearch." The choice of Ni reflects the local rigidity of the PC matching. In this study, we empirically set Ni to 50. The nodal motion vectors were calculated iteratively to obtain the final nodal displacements that were used as the BC in the FE model.

2.B.2.   Prostate tissue modeling—In FE analysis, we assume the prostate is homogeneous. Referring to Khallaghi et al.'s work (Khallaghi et al., 2015a), we set the Young's modulus to be 5kPa and the Poisson's ratio to be 0.49. Neo-Hookean hyperelastic material[39] was used to model the behavior of the prostate. The strain energy function of the neo-Hookean material is defined as[40]:

$$W = C_{10}\big(\bar{I}_1 - 3\big) + \frac{1}{D_1}(J_{el} - 1)^2 \tag{2}$$

where C_{10} is the material constant that controls the shear behavior, D_1 is the material constant that controls the bulk compressibility, $\bar{I}_1$ represents the first strain invariant, and J_{el} is the elastic volume strain. Given the values of Young's modulus and Poisson's ratio, we can derive the values of C_{10} and D_1 using the following equations.

$$C_{10} = \frac{G}{2}, D_1 = \frac{2}{K}, G = \frac{E}{2(1+\nu)}, K = \frac{E}{3(1-2\nu)} \tag{3}$$

where G is the initial shear modulus and K is the bulk modulus, E denotes the Young's modulus, and ν denotes the Poisson's ratio.

2.B.3. FE implementation and nodal displacement calculation—FE models were constructed using commercial FE software (ANSYS 2019 R2, Oxfordshire, UK). The prostate deformation was modeled as a static structural problem with around 1200 nodes and 5800 tetrahedron elements. Stl file of each MRI prostate shape was imported to ANSYS Workbench for subsequent material assignment and meshing. Elastic support was applied on the prostate surface to model surrounding soft tissue support to the prostate. The output was nodal displacement vector with 10 equal temporal substeps. An ANSYS input file for this patient was then generated by ANSYS Workbench. The input file was then modified using MATLAB to apply the calculated nodal displacement BC which was described in Section 2.B.1 by creating a node collection with specified displacement vector for every node. The input file was fed into ANSYS APDL to solve the target FE model. After the model was solved, we recorded the prostate nodal displacement vectors of the whole FE model for all 10 substeps. The displacement vectors were used to generate target PC motion vector for the PCMN to learn. This process is detailed in Section 2.D. One FE example is shown in Fig. 2.

2.C. Point cloud matching network

The goal of PCMN was to take the MRI and CBCT prostate PC as input and predict a dense PC motion vector field which can register the MRI prostate PC to the CBCT prostate PC. The network design was inspired by FlowNet3D that was published by Liu et al. Two major distinctions between our PCMN and FlowNet3D are (a) we encoded biomechanical constraints within the FE-generated target motion vector field, (b) an additional Chamfer surface distance loss was incorporated into the network to learn prostate surface PC matching. The network design of PCMN is shown in Fig. 3. Different from image with regular spatial grid voxels, PC datasets are irregular, spatially unordered, and rotation invariant. Therefore, the neural networks that processes PC need to consider these properties. Traditional convolutional kernels that were widely used in CNNs cannot be directly applied to PC. PC convolutional and up-convolutional operations were used to perform convolution and deconvolution on the scattered PC. For PC motion prediction, a PC embedding layer was used to learn the relationships between the moving PC and fixed PC. Since one-to-one point correspondence is not required and absent, the PC embedding layer used multiple weighted fixed points within a radius of a moving point as soft point correspondence for motion prediction. To consider the unordered-ness and rotation-invariant properties of the PC, a symmetric max pooling operation was used. The max pooling operation was applied on PC within a sphere with varying radius to learn features from both global and local PC. The network can take the input PC as a matrix of N by M (M   3). The M denotes the x, y, z locations of the PC and any additional properties that are specific to this point. In this study, we choose to use a matrix of size N by 7 to represent the PC. The ith point in the MRI PC was rearranged as $v_i^{MR} = \left(x_i^1, y_i^1, z_i^1, x_i^2, y_i^2, z_i^2, m_i^{MR}\right)$, where x_i^1, y_i^1, z_i^1 are

the ith point location in the MRI PC relative to v_c^{MR}, which is the MRI prostate centroid. x_i^2, y_i^2, z_i^2 are the ith point location in the MRI PC relative to v_c^{CT}, which is the CT prostate centroid. The m_i^{MR} is a binary indicator of whether the point belongs to the MRI prostate surface. For CBCT, the ith point in the CBCT PC is expressed as $v_i^{CT} = \left(x_i^3, y_i^3, z_i^3, x_i^4, y_i^4, z_i^4, m_i^{CT}\right)$, where x_i^3, y_i^3, z_i^3 are the ith point location in the CBCT PC relative to v_c^{MR}, x_i^4, y_i^4, z_i^4 are the ith point location in the target PC relative to v_c^{CT}, and m_i^{CT} is a binary indicator of whether the point belongs to the CBCT prostate surface. The MR and CBCT have separate matrices to denote its point configurations, the number of MR points and CBCT points need not to be the same in the training dataset preparation step. In the network training step, a consistent number of 1024 of points were sampled from the MRI and CBCT points.

The predicted PC motion vector was compared to the target FE-generated motion vector to generate the volumetric PC motion loss. The volumetric PC motion loss was a supervised loss since target PC motion was used for the network to learn. Additionally, an unsupervised loss term called the prostate surface distance loss was introduced to encourage the network to predict motion vectors that align the prostate surfaces as well. Chamfer distance loss[41] was used since it was continuous and piecewise smooth with respect to the point location. The final loss of the PCMN is the sum of the volumetric PC motion loss and the prostate surface distance loss,

$$Loss = \text{Avg}\left\{\left(V_p - V_{FE}\right)^2\right\} + \omega \cdot d_{CD}\left(v^m, v^f\right) \tag{4}$$

where V_p denotes the predicted PC motion field, V_{FE} denotes the FE-generated PC motion field, and d_{CD} is the Chamfer distance between the moving v^m and fixed v^f PC.

2.D. Training and testing

The 10 substeps in FE analysis were used to generate a large number of training datasets. With the FE results at the 10 substeps, we can create 10 pairs of artificial training datasets for each patient, including 10 volumetric PC pairs and 10 motion vector fields. The 10 volumetric PC pairs were generated by meshing the 10 MRI and CBCT masks pair that was derived from the FE results. The 10 motion vector fields for the 10 volumetric PC pairs were interpolated from the FE calculated nodal displacements vector. The MRI and CBCT prostate masks were meshed independently so that the number of points in the MRI volumetric PC does not need to be the same to that in the CBCT. This could simplify the meshing for rapid PC generation. For the 50 patients, we have a total of 500 volumetric PC pairs with FE-generated motion vector fields as the network training datasets.

Fivefold cross-validation was used for network training and testing. The 50 patients' datasets were divided into five groups, with 10 datasets in each group. In each experiment, 400 volumetric PC pairs with FE-generated motion vector fields from 40 patients were used to train the network, and the 100 volumetric PC pairs from the rest 10 patients were used to test the network. We repeated the experiment by five times to test all datasets. The PCMN code was implemented using Tensorflow in python. NVIDIA Tesla V100 GPU with 32 GB

memory was used. Batch size was set to 8 to avoid GPU memory overflow. Learning rate was set to 1e-3 during the training. The network was trained for 400 epochs. Training required approximately 1 h. Once trained, the network could predict the PC motion field vector in <1 s.

To show that the PCMN learned from the FE-generated PC motion field, we have shown in Fig. 4(a) the smoothed training and validation loss convergence curves for the volumetric PC motion loss term in Eq. (4). To show the usefulness of the prostate surface distance loss term, its convergence curves are shown in Fig. 4(b).

2.E. Evaluations

The registration results were evaluated using multiple metrics including dice similarity coefficients (DSC), mean surface distance (MSD), center of mass distance (CMD), and target registration error (TRE). Dice similarity coefficients measures the ratio of volume overlap between the CBCT prostate and the deformed MRI prostate. DSC is defined as,

$$DSC = \frac{2 \times |X \cap Y|}{|X| + |Y|} \tag{5}$$

where X and Y represent the volumes of CBCT prostate and the deformed MRI prostate, respectively.

MSD measures the surface distance between the CBCT prostate and the deformed MRI prostate. MSD is defined as,

$$MSD = \frac{1}{|X| + |Y|} \left(\sum_{x \in X} d(x, Y) + \sum_{y \in Y} d(y, X) \right) \tag{6}$$

where $d(x, Y) = min_{y \in Y} x - y_2$. MSD was calculated by averaging the distances for all surface voxels of the prostate. Internal registration accuracy was evaluated using target registration error (TRE). In this study, patients have three prostate fiducial markers implanted within the prostate. The makers show up bright on CBCT and dark on MRI T1. The center locations of the markers were manually identified for TRE calculation. To assess the physical fidelity of the prostate deformation during registration, errors of the normal strains and Jacobian determinants (JDs) were calculated assuming the FE-generated deformation field is ground truth. The Jacobian determinant is calculated by:

$$D = \det(\varepsilon + I) \tag{7}$$

where ϵ denotes the strain tensor of the deformation field, I represents the identity matrix, and $\det(\cdot)$ calculates the determinant of the matrix.

3. RESULTS

For comparison purposes, registration was also performed using coherent point drifting[42] (CPD) prostate surface registration and modality-independent neighborhood descriptor (MIND) registration.[43] For CPD registration, the surface PC motion vector was first

generated by coherently registering the points and then interpolated using thin-plate-spline (TPS) to deform the MRI images to register with CBCT image. For MIND registration, a cross-modality image similarity descriptor was calculated and registered using sum of squared differences (SSD) and Gaussian spatial smoothing. Registration results of one case are shown in Fig. 5. From left to right, columns of Fig. 5 show the CBCT, CPD-registered T1, CPD-registered T2, MIND-registered T1, MIND-registered T2, PCMN-registered T1, and PCMN-registered T2, respectively. Center locations of the three fiducial markers were identified and shown in Fig. 5 with their coordinates. The cyan contours in Fig. 5 represent the fixed CBCT contours while the dashed blue contours represent the deformed MRI contours. We can observe that the CPD surface registration has better contour agreement than the MIND registration and the proposed PCMN registration. The proposed PCMN registration has the best TRE which was 1.28 mm than the CPD registration and the MIND registration, which were 1.55 and 1.42 mm, respectively.

Table I shows the quantitative results for DSC, MSD, and TRE. Both the CPD surface registration and PCMN registration outperformed the rigid registration in terms of all three metrics. The CPD surface registration has slightly better prostate surface alignment between CBCT and MRI than PCMN registration. Since the CPD surface registration method focused solely on surface points and relied purely on TPS interpolation to deform internal prostate, the slightly better surface alignment does not necessarily indicate better intraprostatic deformation. On the contrary, the proposed PCMN took both the surface points and intraprostatic points as input and was trained with biomechanical constraints awareness by using FE-generated intraprostatic motion field. Therefore, the PCMN registration has better TRE than the CPD surface registration. Since MIND registration did not use any contour information, it has worse DSC/MSD than the CPD registration and the PCMN registration. However, the MIND has slightly better TRE than the CPD registration.

Additionally, the JDs and strain tensors were calculated to evaluate the physical fidelity of the deformation field within the prostate. Figure 6 shows the JD map for the FE analysis, CPD surface registration, MIND registration, and the PCMN registration. JD value of greater than 1 means volumetric expansion while JD value lesser than 1 means volumetric shrinkage. We can observe that the CPD and MIND registration have very smooth JD since only smoothness constraints were used during the registration. The PCMN JD map agrees well with that of the FE analysis. No negative JDs were found for all methods. Assuming the FE-generated deformation vector field is ground truth, JD error and normal strain errors were calculated and shown in Table II. The proposed PCMN registration has smaller JD and normal strain errors than the CPD surface registration and MIND registration, which indicates that the proposed PCMN has a more physically realistic deformation.

To visualize the prostate shape alignment and fiducial marker distances after registration, the deformed MRI prostate volumes were overlaid on the fixed CBCT prostate volumes with internal fiducial markers in Fig. 7. Three cases with the lowest, median, and highest TREs for rigid registration were chosen to show the registration performances under good, medium, and poor initialization. For case 2 in Fig. 7, the prostate misalignment was largely caused by prostate shift/rotation since the prostate shapes were nearly consistent between CBCT and MRI and fiducial markers were uniformly shifted/rotated. In this case, the CPD

and PCMN registrations have close TREs since the prostate was mainly shifted/rotated rather than deformed. However, when there were significant prostate deformation and shape discrepancies such as case 1 and case 3 in Fig. 7, the CPD registration has worse TRE than the proposed PCMN registration. This phenomenon is attributed to the biomechanical awareness of the PCMN when deforming the prostate.

4. DISCUSSION

In this study, we focused on MRI-CBCT prostate image registration for potential dose escalation to DIL in photon EBRT and proton therapy. For photon EBRT, studies have shown that the dose to the DIL could be escalated to approximately 125% of the whole prostate prescribed dose and cover 95% of DIL volume before violating OAR dose constraints.[44–46] For proton therapy, Wang et al. have shown that proton pencil beam scanning with simultaneous integrated boost plans has comparable or superior DIL boost dose distribution.[2] Therefore, it is very important to develop an accurate MRI-CT prostate image registration method to improve DIL definition accuracy on CBCT images. Such a registration method could potentially facilitate online adaptive treatment planning and dose accumulation calculation to DIL over the course of treatment. Though tested on MRI-CBCT registration in this study, the proposed method can also be applied to MRI-CT registration to aid treatment planning since CBCT has inferior image quality to CT and thus should be more challenging than CT in the registration.

In this study, we designed the network to perform both prostate surface PC matching and intraprostatic motion prediction. The network could also be used to perform only intraprostatic motions prediction by replacing the 4th to 6th column of network input with known nodal displacement BC. Our preliminary results showed that the inclusion of nodal displacement BC into network input could help improve the PCMN performance. However, the nodal displacement BC needs to be precalculated using prostate surface registration. The method was designed to work on patients without fiducial markers. This is why fiducial markers were used only in the evaluation of our method. In the future, we plan to detect these fiducial markers on CBCT and T1-weighted MRI for initial prostate alignment to improve the registration accuracy.

Given the fact that the original CBCT image resolution was $1.0 \times 1.0 \times 2.0$ mm^3, one-pixel error in each direction would result in a TRE of 2.45 mm. Therefore, the mean TRE of 2.68 mm is quite good. However, the standard deviation of 1.91 mm is a little large. Our TRE results indicate that 15.8% of cases would have TRE <4.5 mm. We have investigated the cases with large TRE values. The main reason for the large TRE was the inaccurate contour of the CBCT prostate due to poor image quality, which is one limitation of the study since the PCMN relies on accurate contour to perform registration. We did not perform any manual contour correction in this study. However, manual contours corrections may be necessary depending on the image quality of the CBCT. The last fraction CBCT may have the largest possibility of fiducial marker migration, which could cause TRE inaccuracies. However, Kupelian et al.[47] investigated 56 prostate patients with 168 markers and concluded that none of the 168 markers showed evidence of consistent migration throughout the course

of treatment, and that the marker position variation from day to day was caused by prostate deformation rather than marker migration.

Out of the 50 patients, 35 patients have undergone androgen deprivation therapy (ADT) from 4 months to 2 yr at different time point throughout their treatments. The prostate volume could change during the treatment. In this study, the MRI was taken on the same day as the CT simulation. The time span between the MRI scanning and the CBCT scanning ranges from 20 to 40 days depending on the patients' prescription. The prostate volume was not expected to change dramatically within this narrow time-frame. The proposed method was designed to handle expected prostate volume discrepancies between the MRI and CBCT due to auto-segmentation uncertainties. However, patients with irregular deformation or prostate volume change could affect the registration accuracy. To adapt the proposed framework to these patients, patients of such cases could be included in the training datasets. As a common practice, patients should be educated on bowel and bladder preparation to reduce the possibility of irregular prostate deformation.

5. CONCLUSIONS

We developed a new framework to accurately register the mpMRI to CBCT images for external beam radiotherapy of prostate cancer. The proposed method could be used to aid DIL delineation on CBCT, prostate adaptive treatment planning, dose escalation to DIL, and dose monitoring.

## ACKNOWLEDGMENTS

REFERENCES

1. Weir HK, Thompson TD, Soman A, Moller B, Leadbetter S. The past, present, and future of cancer incidence in the United States: 1975 through 2020. Cancer. 2015;121:1827–1837. [PubMed: 25649671]

2. Wang T, Zhou J, Tian S, et al. A planning study of focal dose escalationsto multiparametric MRI-defined dominant intraprostatic lesions in prostate proton radiation therapy. Br J Radiol. 2020;93:20190845. [PubMed: 31904261]

3. von Eyben FE, Kiljunen T, Kangasmaki A, Kairemo K, von Eyben R,Joensuu T. Radiotherapy boost for the dominant intraprostatic cancer lesion-a systematic review and meta-analysis. Clin Genitourin Cancer. 2016;14:189–197. [PubMed: 26768965]

4. Ciardo D, Jereczek-Fossa BA, Petralia G, et al. Multimodal image registration for the identification of dominant intraprostatic lesion in highprecision radiotherapy treatments. Br J Radiol. 2017;90:20170021. [PubMed: 28830203]

5. Lee J, Carver E, Feldman A, Pantelic MV, Elshaikh M, Wen N. Volumetric and voxel-wise analysis of dominant intraprostatic lesions on multiparametric MRI. Front Oncol. 2019;9:616. [PubMed: 31334128]

6. Zamboglou C, Klein CM, Thomann B, et al. The dose distribution indominant intraprostatic tumour lesions defined by multiparametric MRI and PSMA PET/CT correlates with the outcome in patients treated with primary radiation therapy for prostate cancer. Radiat Oncol. 2018;13:65. [PubMed: 29650029]

7. Huang E, Dong L, Chandra A, et al. Intrafraction prostate motion duringIMRT for prostate cancer. Int J Radiat Oncol Biol Phys. 2002;53:261–268. [PubMed: 12023128]

8. Dean CJ, Sykes JR, Cooper RA, et al. An evaluation of four CT-MRIco-registration techniques for radiotherapy treatment planning of prone rectal cancer patients. Br J Radiol. 2012;85:61–68. [PubMed: 22190750]

9. Rivest-Henault D, Dowson N, Greer PB, Fripp J, Dowling JA. Robustinverse-consistent affine CT-MR registration in MRI-assisted and MRI-alone prostate radiation therapy. Med Image Anal. 2015;23:56–69. [PubMed: 25966468]

10. McLaughlin PW, Narayana V, Kessler M, et al. The use of mutual information in registration of CT and MRI datasets post permanent implant. Brachytherapy. 2004;3:61–70. [PubMed: 15374537]

11. Commandeur F, Simon A, Mathieu R, et al. MRI to CT prostate registration for improved targeting in cancer external beam radiotherapy. IEEE J Biomed Health Inform. 2017;21:1015–1026. [PubMed: 27333613]

12. Kunogi H, Hojo H, Wakumoto Y, et al. A new two-step accurate CT-MRI fusion technique for post-implant prostate cancer. J Contemp Brachytherapy. 2015;7:117–121. [PubMed: 26034491]

13. Parker CC, Damyanovich A, Haycocks T, Haider M, Bayley A, Catton CN. Magnetic resonance imaging in the radiation treatment planning of localized prostate cancer using intra-prostatic fiducial markers for computed tomography co-registration. Radiother Oncol. 2003;66:217–224. [PubMed: 12648794]

14. Cao X, Yang J, Gao Y, Wang Q, Shen D. Region-adaptive deformableregistration of CT/MRI pelvic images via learning-based image synthesis. IEEE Trans Image Process. 2018;27:3500–3512.

15. Fu Y, Lei Y, Zhou J, et al. Non-Rigid MRI-CT Image Registration with Unsupervised Deepd learning-Based Deformation Prediction. Vol 11313 SPIE; 2020.

16. Khallaghi S, Sanchez CA, Rasoulian A, et al. Statistical biomechanicalsurface registration: application to MR-TRUS fusion for prostate interventions. IEEE Trans Med Imaging. 2015;34:2535–2549. [PubMed: 26080380]

17. Khallaghi S, Sanchez CA, Rasoulian A, et al. Biomechanically constrained surface registration: application to MR-TRUS fusion for prostate interventions. IEEE Trans Med Imaging. 2015;34:2404–2414. [PubMed: 26054062]

18. van de Ven WJ, Hu Y, Barentsz JO, Karssemeijer N, Barratt D, Huisman HJ. Biomechanical modeling constrained surface-based image registration for prostate MR guided TRUS biopsy. Med Phys. 2015;42:2470–2481. [PubMed: 25979040]

19. Yang X, Akbari H, Halig L, Fei B. 3D non-rigid registration using surface and local salient features for transrectal ultrasound image-guided prostate biopsy. Proc SPIE Int Soc Opt Eng. 2011;7964:79642v.

20. Hentschel B, Oehler W, Strauss D, Ulrich A, Malich A. Definition of theCTV prostate in CT and MRI by using CT-MRI image fusion in IMRT planning for prostate cancer. Strahlenther Onkol. 2011;187:183–190. [PubMed: 21347638]

21. Fu Y, Lei Y, Wang T, et al. Pelvic multi-organ segmentation on conebeam CT for prostate adaptive radiotherapy. Med Phys. 2020;47:3415–3422. [PubMed: 32323330]

22. Zhang J, Wang J, Wang X, Feng D. The adaptive FEM elastic model formedical image registration. Phys Med Biol. 2014;59:97–118. [PubMed: 24334618]

23. Velec M, Moseley J, Svensson S, Hardemark B, Jaffray D, Brock K. Validation of biomechanical deformable image registration in the abdomen, thorax, and pelvis in a commercial radiotherapy treatment planning system. Med Phys. 2017;44:3417.

24. Bharatha A, Hirose M, Hata N, et al. Evaluation of three-dimensionalfinite element-based deformable registration of pre- and intraoperative prostate imaging. Med Phys. 2001;28:2551–2560. [PubMed: 11797960]

25. Alterovitz R, Goldberg K, Pouliot J, et al. Registration of MR prostateimages with biomechanical modeling and nonlinear parameter estimation. Med Phys. 2006;33:446–454. [PubMed: 16532952]

26. Hu Y, Morgan D, Ahmed HU, et al. A statistical motion model based onbiomechanical simulations for data fusion during image-guided prostate interventions. Med Image Comput Comput Assist Interv. 2008;11:737–744. [PubMed: 18979812]

27. Hu Y, Ahmed HU, Taylor Z, et al. MR to ultrasound registration forimage-guided prostate interventions. Med Image Anal. 2012;16:687–703. [PubMed: 21216180]

28. Zhong H, Wen N, Gordon JJ, Elshaikh MA, Movsas B, Chetty IJ. Anadaptive MR-CT registration method for MRI-guided prostate cancer radiotherapy. Phys Med Biol. 2015;60:2837–2851. [PubMed: 25775937]

29. Boubaker MB, Haboussi M, Ganghoffer JF, Aletti P. Finite element simulation of interactions between pelvic organs: predictive model of the prostate motion in the context of radiotherapy. J Biomech. 2009;42:1862–1868. [PubMed: 19559437]

30. Lei Y, Fu Y, Wang T, et al. Deep learning in multi-organ segmentation. ArXiv; 2020;abs/2001.10619.

31. Fu Y, Lei Y, Wang T, Curran WJ, Liu T, Yang X. Deep learning in medical image registration: a review. Phys Med Biol. 2020;65:20TR01.

32. Wang T, Lei Y, Fu Y, Curran WJ, Liu T, Yang X. Medical imaging synthesis using deep learning and its clinical applications: a review; 2020.

33. Qi C, Su H, Mo K, Guibas LJ. PointNet: deep learning on point sets for3D classification and segmentation. 2017 IEEE Conference on Computer Vision and Pattern Recognition (CVPR); 2016:77–85.

34. Qi CR, Yi L, Su H, Guibas LJ. PointNet++: deep hierarchical feature learning on point sets in a metric space. Paper presented at: NIPS; 2017.

35. Liu X, Qi CR, Guibas LJ. FlowNet3D: learning scene flow in 3D pointclouds. Paper presented at: CVPR; 2018.

36. Aoki Y, Goforth H, Srivatsan RA, Lucey S. PointNetLK: robust & efficient point cloud registration using PointNet. Paper presented at: CVPR; 2019.

37. Wang B, Lei Y, Tian S, et al. Deeply supervised 3D fully convolutionalnetworks with group dilated convolution for automatic MRI prostate segmentation. Med Phys. 2019;46:1707–1718. [PubMed: 30702759]

38. Audenaert EA, Van Houcke J, Almeida DF, et al. Cascaded statisticalshape model based segmentation of the full lower limb in CT. Comput Methods Biomech Biomed Eng. 2019;22:644–657.

39. Shahzad M, Kamran A, Siddiqui MZ, Farhan M. Mechanical characterization and FE modelling of a hyperelastic material; 2015.

40. Pence TJ, Gou K. On compressible versions of the incompressible neo-Hookean material. Math Mech Solids. 2015;20:157–182.

41. Fan H, Su H, Guibas LJ. A point set generation network for 3D objectreconstruction from a single image. 2017 IEEE Conf Comp Vis Pattern Recogn; 2016:2463–2471.

42. Bernhard S, John P, Thomas H. Non-rigid point set registration: coherent point drift. In: Advances in Neural Information Processing Systems 19: Proceedings of the 2006 Conference MITP; 2007:1.

43. Heinrich MP, Jenkinson M, Bhushan M, et al. MIND: modality independent neighbourhood descriptor for multi-modal deformable registration. Med Image Anal. 2012;16:1423–1435. [PubMed: 22722056]

44. Oermann EK, Slack RS, Hanscom HN, et al. A pilot study of intensitymodulated radiation therapy with hypofractionated stereotactic body radiation therapy (SBRT) boost in the treatment of intermediate- to high-risk prostate cancer. Technol Cancer Res Treat. 2010;9:453–462. [PubMed: 20815416]

45. Murray LJ, Lilley J, Thompson CM, et al. Prostate stereotactic ablative radiation therapy using volumetric modulated arc therapy to dominant intraprostatic lesions? Int J Radiat Oncol Biol Phys. 2014;89: 406–415. [PubMed: 24685447]

46. Housri N, Ning H, Ondos J, et al. Parameters favorable to intraprostaticradiation dose escalation in men with localized prostate cancer. Int J Radiat Oncol Biol Phys. 2011;80:614–620. [PubMed: 20932672]

47. Kupelian PA, Willoughby TR, Meeks SL, et al. Intraprostatic fiducialsfor localization of the prostate gland: monitoring intermarker distances during radiation therapy to test for marker stability. Int J Radiat Oncol Biol Phys. 2005;62:1291–1296. [PubMed: 16029784]
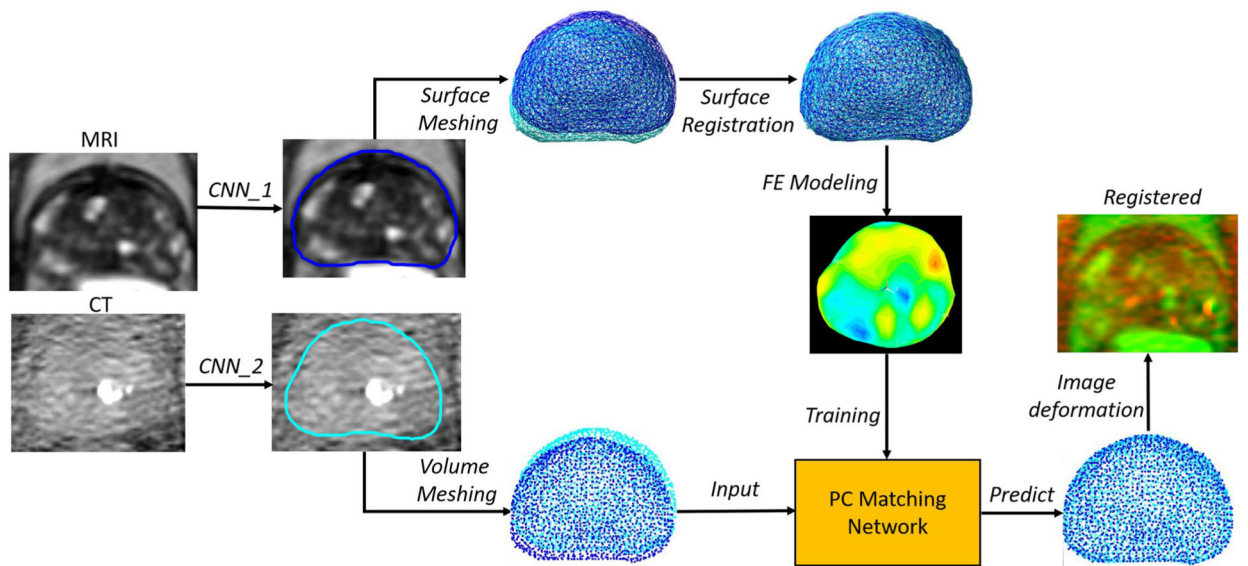
Fig. 1.
Workflow of the training and testing of the proposed point cloud matching network. Blue
and cyan colors represent the magnetic resonance imaging and computed tomography
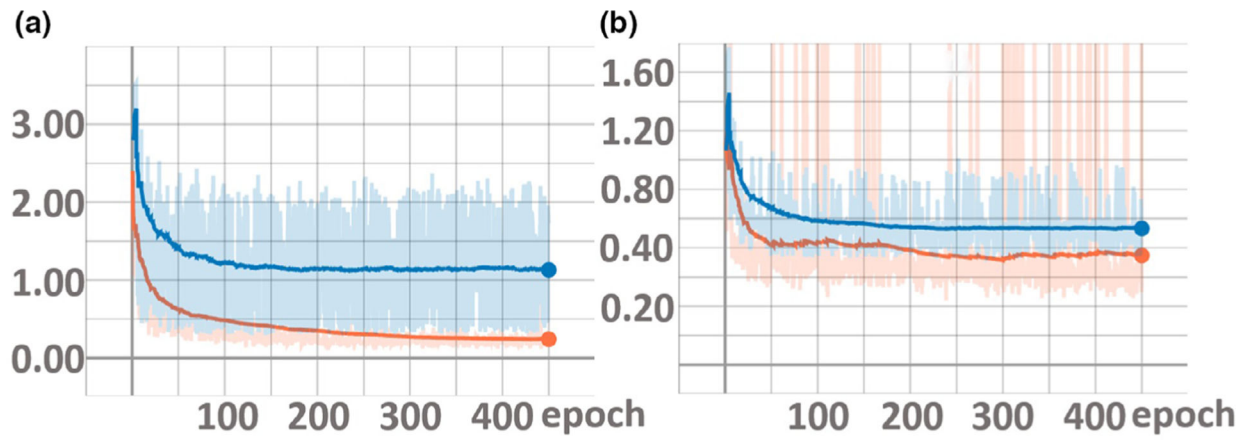prostates, respectively.
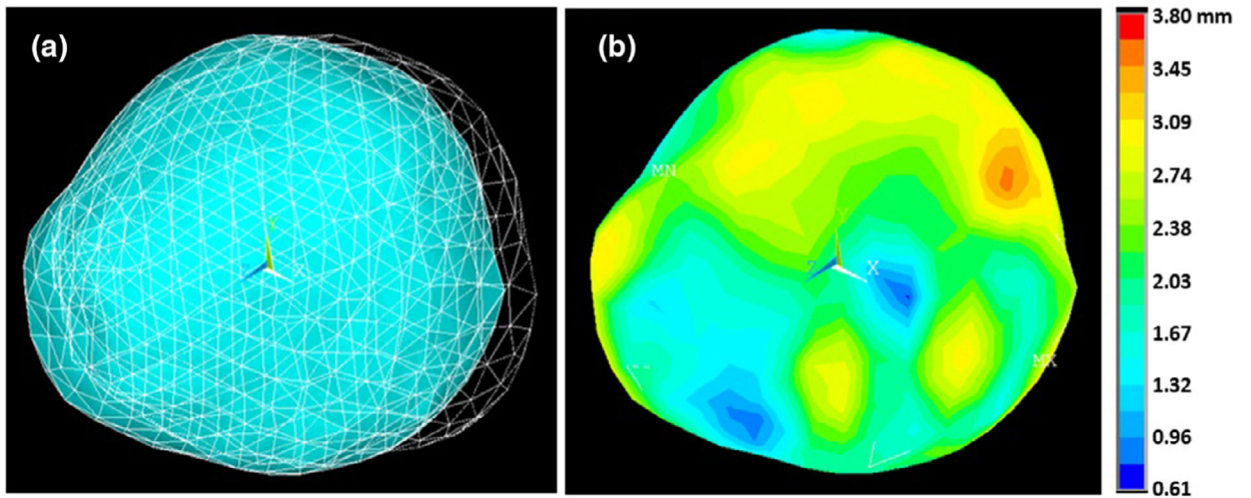
Fig. 2.
Finite element analysis results for one case a: Original and deformed prostate shapes in, b: Magnitude contour of nodal displacement vector plotted on deformed shape.
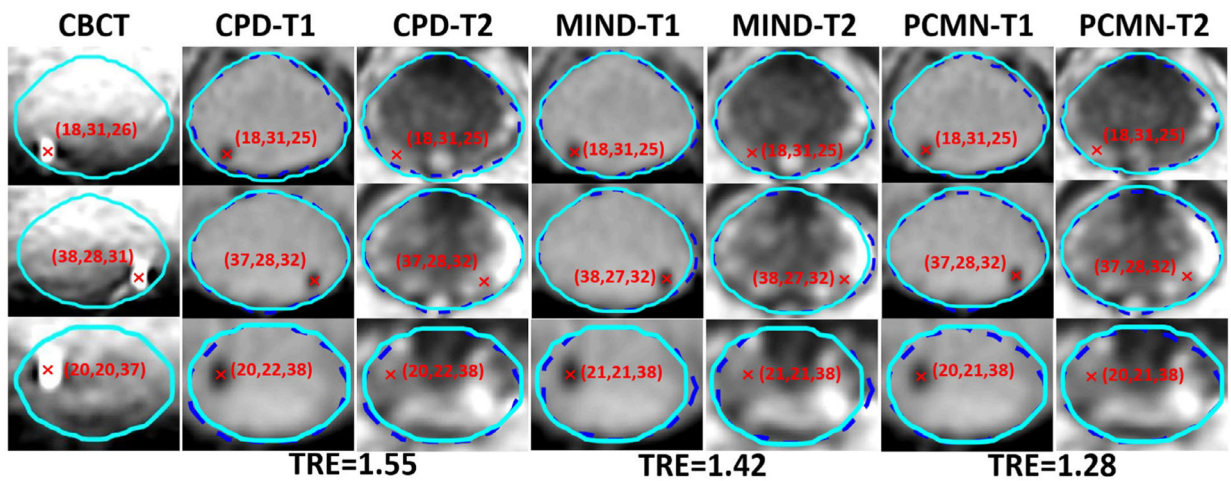
PCMN
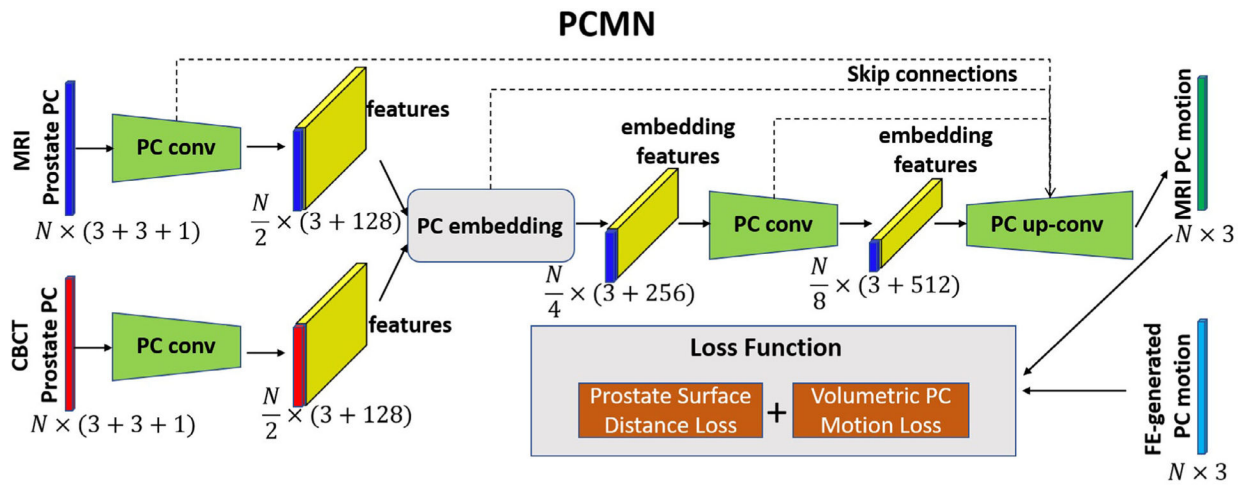
Fig. 3.
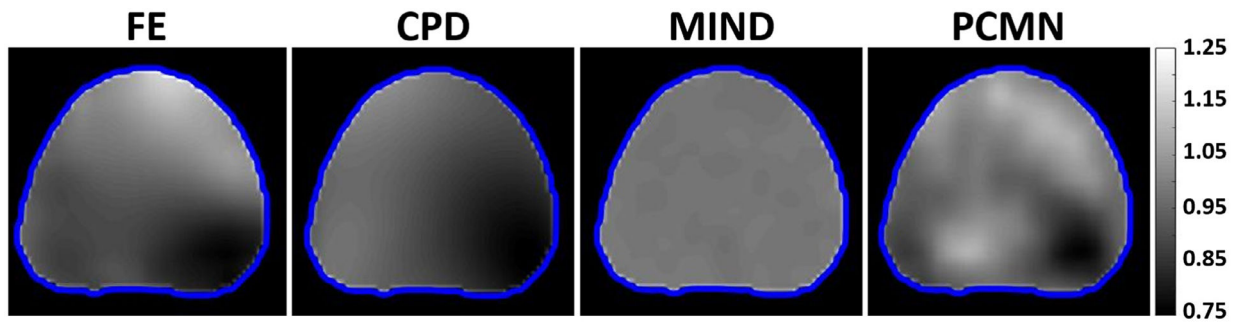Network design of the point cloud matching network.

Fig. 4.
Smoothed training and validation convergence curves. Validation loss is shown in blue color while training loss is shown in orange color. A: Volumetric PC motion loss, B: Prostate surface distance loss.

Fig. 5.
CBCT and deformed magnetic resonance imaging (MRI) T1 and T2 images. CBCT prostate is shown in cyan solid contour. MRI prostate is shown in blue-dashed contour. Center locations of markers are shown by red crosses their coordinates. From left to right columns show CBCT, coherent point drifting (CPD)-registered T1, CPD-registered T2, modality-independent neighborhood descriptor (MIND)-registered T1, MIND-registered T2, point cloud matching network (PCMN)-registered T1, and PCMN-registered T2, respectively. Target registration errors are in mm.

Fig. 6.
Left to right: Jacobian determinant maps for finite element analysis, coherent point drifting surface registration, modality-independent neighborhood descriptor registration, and point cloud matching network registration.
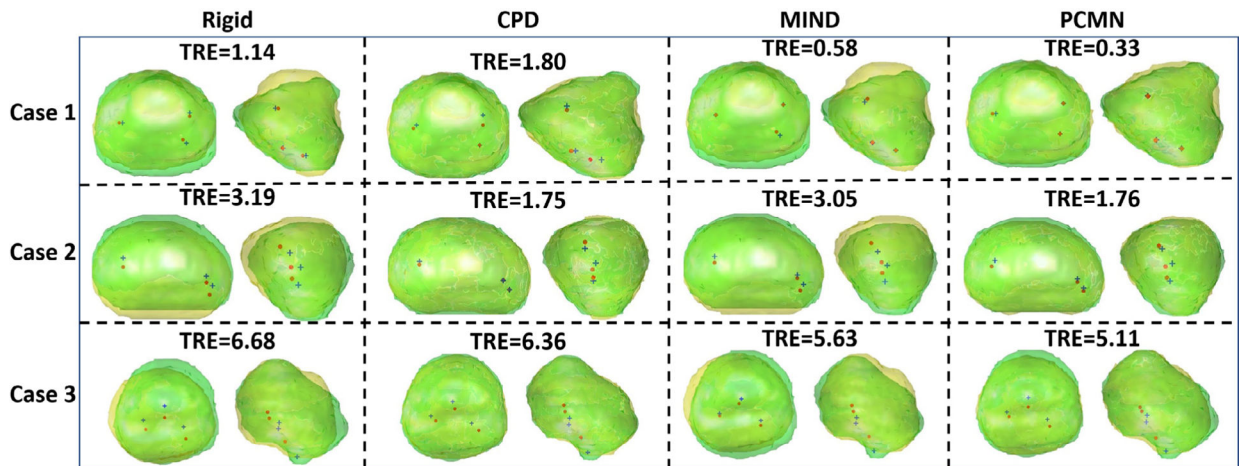
Fig. 7.
Prostate alignment for three cases using image intensity-based rigid registration, coherent point drifting surface registration, modality-independent neighborhood descriptor registration, and the proposed point cloud matching network registration. Cases 1, 2, and 3 represent three cases with small, intermediate, and large target registration error (TREs). Fixed CBCT prostate are shown in green with blue "+" fiducial markers. Deformed MRI prostate are shown in yellow with red dot fiducial markers. TREs are in mm.

Table I.

Numerical comparisons among image intensity-based rigid registration (Rigid), coherent point drifting (CPD) surface registration (CPD), MIND registration, and the proposed method (PCMN).

Method	DSC	MSD (mm)	TRE (mm)
Rigid	0.86 ± 0.04	2.21 ± 0.36	3.78 ± 2.72
CPD	$\mathbf{0.94 \pm 0.01}$	$\mathbf{1.58 \pm 0.06}$	3.13 ± 2.06
MIND	0.89 ± 0.03	1.98 ± 0.07	3.03 ± 1.93
PCMN	0.93 ± 0.01	1.66 ± 0.10	$\mathbf{2.68 \pm 1.91}$

Values are shown in mean ± std with best mean values shown in bold.

Table II.

Mean absolute error of JD and normal strain between the FE analysis and prediction for coherent point drifting (CPD) surface registration, MIND registration, and PCMN registration.

	JD	E_{xx}	E_{yy}	E_{zz}
CPD	0.14 ± 0.08	0.09 ± 0.03	0.08 ± 0.02	0.10 ± 0.07
MIND	0.12 ± 0.05	0.08 ± 0.02	0.06 ± 0.02	0.10 ± 0.05
PCMN	**0.11 ± 0.05**	**0.06 ± 0.02**	**0.06 ± 0.02**	**0.06 ± 0.02**

Values: Mean ± Std. Smallest errors are shown in bold.